



Full Text View

[Volume 30, Issue 2 \(February 2000\)](#)

Journal of Physical Oceanography

Article: pp. 269–293 | [Abstract](#) | [PDF \(620K\)](#)

Low-Frequency Variability in the Wind-Driven Circulation

S. P. Meacham

Department of Oceanography, The Florida State University, Florida

(Manuscript received June 13, 1997, in final form February 9, 1999)

DOI: 10.1175/1520-0485(2000)030<0269:LFVITW>2.0.CO;2

ABSTRACT

The origins of low-frequency variability in a simple homogenous ocean model, forced by a double gyre Ekman suction, are examined numerically. It is found that irregular, large amplitude vacillations in the structure of the circulation typify the behavior of such a model when it is forced sufficiently strongly. These oscillations are associated with order-one changes in the size and transport of the inertial recirculation gyres that lie near the western boundary. It is suggested that this behavior arises as a result of a subcritical homoclinic bifurcation. The aperiodic solutions do not exhibit a strong tendency to linger near any of the simpler unstable solutions that were found for this system. Instead, the latter solutions appear to constrain the aperiodic solutions, confining them to a limited region of phase space for a range of values of the Munk boundary layer scale δ_M . The form of the aperiodic solutions suggests that there may be an interesting unstable solution that could not be isolated. This solution would consist of an oscillation of the dipolar structure formed by the pair of recirculation gyres. The behavior described appears robust to the addition of a degree of asymmetry in the forcing. Similar large amplitude, low frequency fluctuations in the circulation are also found in a baroclinic double gyre model. In the baroclinic model, these fluctuations occur on a decadal timescale and are sufficiently large that they must be considered a potential component mechanism for some of the decadal climate oscillations seen in the extratropics.

Table of Contents:

- [Introduction](#)
- [Models](#)
- [Methods](#)
- [Results](#)
- [Discussion](#)
- [REFERENCES](#)
- [FIGURES](#)

Options:

- [Create Reference](#)
- [Email this Article](#)
- [Add to MyArchive](#)
- [Search AMS Glossary](#)

Search CrossRef for:

- [Articles Citing This Article](#)

Search Google Scholar for:

- [S. P. Meacham](#)

1. Introduction

The coupled atmosphere–ocean system exhibits variability on many timescales, from shorter than a day to the very low frequency variability associated with ice ages. A crucial set of timescales are those that stretch from a few years to a few decades. An understanding of variability on these timescales would improve the ability to make climate forecasts. In addition, when attempting to search for evidence of anthropogenic modification of the earth's climate, natural variability at these timescales has the potential to both mask such changes and be mistaken for such changes.

Evidence of variability in this band of timescales is abundant. In the tropical atmosphere and ocean, the signature of the ENSO cycle is a prime example of variability with a timescale of a few years. In the extratropics, both the atmosphere and the ocean show multiyear variability. An atmospheric example is the irregular, roughly decadal oscillation of the North Atlantic Oscillation index (e.g., [Hurrell 1996](#)), while in the ocean there is significant evidence of decadal and longer variability in midlatitude sea surface temperature (e.g., [Kushnir 1994](#); [Hansen and Bezdek 1996](#)).

There are many potential sources of low-frequency variability in the coupled ocean–atmosphere system. Considerable attention has been focused recently on oscillations that involve the deep thermohaline circulation. However, the upper ocean wind-driven circulation, either considered by itself or linked to a time-dependent atmosphere, has the potential to exhibit low-frequency variability. In this paper, we shall demonstrate some of the low-frequency variability exhibited by double gyre models of the wind-driven circulation when the wind stress is held steady. We shall show that there are regimes of large amplitude, low-frequency variability that appear to be associated with homoclinic bifurcations (a type of global bifurcation, unlike the more usual form of normal-mode oscillatory instabilities that arise through local bifurcations) and that the extent of this variability is constrained by the proximity, in phase space, of unstable but simple solutions of the equations governing the flow. In particular, we will see solutions that wander in a region bounded by three unstable periodic oscillations.

The notion of a homoclinic orbit can be illustrated by the example of a solitary wave. A homoclinic orbit is a trajectory in phase space that starts and ends on a simple invariant set, such as a fixed point (i.e., a steady state), as $t \rightarrow \pm\infty$. As such, its structure depends not only on the physical properties of the system in the vicinity of the steady state but along the entire homoclinic trajectory, which typically moves a significant distance from the fixed point. Consider a soliton on the surface of a thin layer of fluid in a channel as it approaches and then passes by a given point. A large time before the arrival of the soliton, the water depth is very close to steady; there is only an exponentially small rate of change. As the soliton approaches, the water level begins to rise at a more perceptible rate until a large displacement is seen as the soliton goes by. After the soliton has passed, the water level falls, rapidly at first and then ever more slowly until, a long time after the passage of the soliton, the water level is again approximately steady with its original depth. The soliton can be thought of as a nonlinear disturbance to a steady state. If one linearizes about the steady state that is approached as $t \rightarrow \pm\infty$, the result will be a small amplitude sinusoidal wave. This is clearly not the structure of the soliton. During the passage of the soliton, the system made a large excursion away from the steady state and then returned to it. In the appropriate dynamical representation of the soliton, this is a homoclinic orbit. To return to the phase space of our barotropic GCM, suppose we have an unstable fixed point. A linear analysis around the fixed point will determine a set of stable eigenvectors and a set of unstable eigenvectors. Locally, the former span the stable subspace of the domain around the fixed point and the latter, the unstable subspace. The continuation of these subspaces to larger distances from the fixed point are respectively the stable and unstable manifolds. While flat in the neighborhood of the fixed point where the linearization approximation holds, these manifolds are typically curved at larger distance. If these manifolds touch as we change some parameter of the system, for example, the Munk boundary layer scale δ_M , then a homoclinic orbit (or set of homoclinic orbits) will appear—a curve that lies in both the stable and unstable manifolds and both leaves and approaches the fixed point. Beyond this critical value of δ_M , several things may happen depending on the linear eigenvalues of the fixed point. [See [Glendinning \(1994\)](#); or [Guckenheimer and Holmes \(1983\)](#), for details.] One possibility is the appearance of a strange attractor. In such a case, close to the critical δ_M , trajectories on the strange attractor consist of loops that individually resemble the path of the homoclinic orbit. The numerical evidence that we present below suggests that such a homoclinic bifurcation to a strange attractor occurs in the barotropic double-gyre model and gives rise to irregular low-frequency vacillations. A physical explanation of these vacillations is suggested in [sec-tion 5](#).

The steady states of a homogeneous ocean of uniform depth, forced with a purely antisymmetric double-gyre wind stress, were examined in some detail by [Cessi and Ierley \(1995, CI hereafter\)](#). They documented the existence of several stationary bifurcations that gave rise to a multiplicity of possible stationary circulations. [Primeau \(1998, P hereafter\)](#) has made calculations for a homogeneous ocean subject to slightly different boundary conditions and found behavior similar to that seen by [Cessi and Ierley \(1995\)](#). [Jiang et al. \(1995, JJG hereafter\)](#) considered a similar problem but in a shallow-water reduced-gravity model. [The locations of the bifurcations seen by Jiang et al. were shifted in parameter space as a result of inadequate resolution, as noted by [Jones et al. \(1997\)](#), but this does not affect the *form* of the early bifurcations.] This type of model does not possess the meridional symmetry of the quasigeostrophic problem, and consequently the stationary bifurcations become saddle-node bifurcations rather than the pitchfork bifurcations of the symmetric quasigeostrophic theory. These “perturbed pitchfork” bifurcations are the generic continuations of the nongeneric pitchfork bifurcations. When the deviation from symmetry is small, the combination of a saddle-node bifurcation and a nearby continuous branch of solutions looks very similar to a pitchfork bifurcation of the symmetric problem. The difference between the two cases increases continuously as the departure from symmetry is increased. Thus, the symmetric quasigeostrophic problem provides a useful model of both the asymmetric shallow water problem and the asymmetrically forced quasigeostrophic (QG) problem when the departures from symmetry are sufficiently small. The existence of multiple states and their stability properties are robust to small perturbations away from meridional symmetry.¹

In barotropic and quasigeostrophic baroclinic single-gyre models, [Meacham and Berloff \(1997, MB hereafter\)](#) and [Berloff](#)

and Meacham (1998, BM hereafter) showed that as the dissipation in the flow is reduced, simple time-dependent solutions branch off from the stationary circulation solutions. At first, these take the form of periodic oscillations and their origins lie in the linear instabilities of the steady circulation. As dissipation is reduced further, the complexity of the time-dependent solutions increases and one eventually reaches a chaotic regime. This transition to chaotic motion is accompanied by the advent of low-frequency variability. However, it does not appear to be associated with a homoclinic bifurcation. Instead, a sequence of two or three Hopf bifurcations gives rise to an unstable toroidal attractor that gives way to a strange attractor.

The time-dependent behavior of a typical ocean general circulation model (OGCM) is quite complicated. The examples in the works cited (e.g., CI, P, JIG, MB, and BM) demonstrate that bifurcation theory, in combination with classical linear stability theory, can provide a framework for understanding how this complicated time dependence arises. In a model ocean, whether numerical or in the laboratory, as the degree of nonlinearity of the system is increased, either by increasing the strength of the forcing or decreasing the strength of the frictional dissipation, the model undergoes a succession of bifurcations and, as it does so, the evolution of the circulation becomes progressively more complicated. For example, unpublished laboratory modeling by R. Krishnamurti shows changes in the regime of a barotropic model ocean consistent with a Hopf bifurcation, while numerical experiments show transitions to strange attractors (e.g., MB).² In general, some of the simpler solutions seen at low nonlinearity persist as unstable solutions at higher nonlinearity. (Some can be lost through saddle-node bifurcations, e.g., CI.) Considered as a dynamical system, the phase space of an OCGM is very large, though finite. The generic behavior of simple solutions in nonsymmetric dynamical systems is that they undergo bifurcations of finite codimension, typically a codimension of one. This means that at each bifurcation, a simple solution typically loses stability in only one or two dimensions of the large-dimensional phase space. This makes it likely that, when an OGCM is moderately nonlinear and the resulting time dependence of the model is highly aperiodic, simple solutions will exist that are unstable (repelling) in a relatively small fraction of the dimensions in the available phase space and stable (attracting) in the remaining directions. This conjecture (a conjecture because it is unknown whether there are situations in OCGMs in which an infinite sequence of bifurcations occurs over a finite range of Reynolds number) raises the possibility that when the behavior of the OGCM is aperiodic, the evolution of the model may nevertheless be influenced by unstable simple solutions that temporarily attract the solution trajectory before spitting it out along an unstable direction (cf. [Legras and Ghil 1985](#)). We will start with this hypothesis and see whether the evidence, obtained in the work described below, supports or opposes it. The work reported in this paper does three things: (i) describes some of the simple solutions of a barotropic double-gyre model of the wind-driven circulation, extending the work of CI to time-dependent solutions, (ii) demonstrates the appearance of a type of low-frequency variability in both barotropic and baroclinic models of double gyre circulations, and (iii) demonstrates an empirical relation between an aperiodic solution of the barotropic double-gyre problem that exhibits low-frequency variability and several of the simpler solutions.

The existence of a transition from a steady circulation to a time-dependent circulation as the degree of nonlinearity of the model is increased was noted by [Bryan \(1963\)](#), [Holland and Lin \(1975a,b\)](#), and [Holland \(1978\)](#). Later investigations have noted the presence of low-frequency components in the time-dependent behavior of a steadily forced OGCM. [Holland \(1978\)](#), using a two-layer QG model forced with a steady wind stress, noted considerable variability at timescales beyond 5 months. [Holland and Haidvogel \(1981\)](#) also reported results from a two-layer QG model with steady wind-stress forcing. They noted that in a single-gyre model, as the Reynolds number was increased, the first form of time dependence encountered was a mesoscale instability of the steady circulation that gave rise to a limit cycle with a period of $O(30)$ days. At a higher Reynolds number, this underwent a secondary oscillatory instability to produce a quasiperiodic state in which a vacillation cycle of $O(500)$ days was superimposed on the original $O(30)$ days limit cycle. The results reported by [Holland and Haidvogel \(1981\)](#) are consistent with the notion that the vacillation cycle occurs as a result of a secondary Hopf bifurcation (a secondary oscillatory instability in which a conjugate pair of eigenvalues of the linearized problem cross the imaginary axis). This was confirmed by [Berloff and Meacham \(1998\)](#), who traced out several secondary instabilities of this type in a problem similar to that considered by [Holland and Haidvogel \(1981\)](#). [Cox \(1987\)](#), in a study of a steadily forced, but thermodynamically active, primitive equation model, observed variability at three dominant timescales: around 50 days, roughly 1.1 years, and between 4 and 4.5 years. The former was associated with mesoscale variability, while the latter was associated with fluctuations in the depth and shape of the thermocline and involved large-scale signals with the signature of first mode baroclinic waves. The period 4–4.5 yr was determined from the observation of model output of six years duration, so it is not clear whether this is a cycle that is close to periodic or highly irregular, nor is it clear whether coupling to the atmosphere via the surface heat flux is a vital part of this cycle. [Moro \(1990\)](#), in a study of the behavior of an asymmetrically forced double-gyre barotropic model, noted a variety of spectral peaks at timescales ranging from $O(50)$ days to $O(1600)$ days, but their dependence on the Reynolds number of the model is unclear. [Berloff and Meacham \(1998\)](#), in their study of a two-layer, single-gyre, QG model, noted the appearance of timescales as long as $O(1000)$ days and $O(1600)$ days as a result of secondary Hopf bifurcations.

A study that lends some support to the existence of simpler structure within complicated aperiodic time-dependent solutions of the wind-driven circulation was made by [McCalpin and Haidvogel \(1996\)](#). They considered a reduced-gravity, QG, double-gyre model. Taking the time series of basin-integrated kinetic energy from a long run and making a histogram of the distribution of values of the kinetic energy, they noted three statistical modes: at high, intermediate, and low energy. By making short-term averages of the streamfunction pattern when the flow energy was close to each of these modal values, they found that the three energy levels corresponded to distinct flow regimes in which the intergyre jet had different zonal

extents and different degrees of straightness. What remains unanswered is whether these statistical modes correspond to simple, though unstable, solutions of the equations of motion.

In [sections 2](#) and [3](#), we summarize the circulation models used in this paper and describe the methods used to analyze the behavior of the models. In [section 4](#), we describe the behavior of a barotropic, symmetric, double-gyre circulation model and compare some aspects of its behavior with results from an asymmetrically forced barotropic model and a baroclinic model. A discussion of the results is presented in [section 5](#).

One of the main results to emerge in [section 4](#) is the appearance of an irregular, low-frequency vacillation of the barotropic double-gyre circulation. Though its average period is of the same order of magnitude as some of the vacillation cycles that occur as a result of secondary instabilities in the two-layer, single-gyre models noted above, its structure, and the underlying mechanism, appears to be distinct from the cycles seen in [Holland and Haidvogel \(1981\)](#) and [Berloff and Meacham \(1998\)](#).

2. Models

For most of the work reported here, a barotropic ocean model was used. The governing equation is the potential vorticity equation written in terms of a barotropic streamfunction ψ ,

$$\partial_t \nabla^2 \psi + J(\psi, \nabla^2 \psi) + \beta \psi_x = \nu \nabla^4 \psi + \frac{f w_E}{H}. \quad (1)$$

Here f and β are the planetary vorticity and its gradient ν is a uniform eddy viscosity, H is the ocean depth, and the Ekman suction velocity is

$$w_E = Ww(y/L),$$

where L is the zonal width of the basin, W is a dimensional scale for the vertical Ekman velocity, and w is a dimensionless function describing the spatial pattern of the vertical Ekman velocity.

We nondimensionalize by scaling x and y with L , t with $(\beta L)^{-1}$, and ψ with $(fWL/\beta H)$, and introduce the dimensional Munk and inertial boundary layer scales,

$$\delta_M^* = \left(\frac{\nu}{\beta} \right)^{1/3}, \quad \delta_I^* = \left(\frac{fW}{\beta^2 H} \right)^{1/2}$$

together with their dimensionless counterparts

$$\delta_M = \delta_M^*/L, \quad \delta_I = \delta_I^*/L.$$

The nondimensional vorticity equation is then

$$\partial_t \nabla^2 \psi + \delta_I^2 J(\psi, \nabla^2 \psi) + \psi_x = \delta_M^3 \nabla^4 \psi + w(y). \quad (2)$$

We will also discuss results from a two-layer, quasigeostrophic baroclinic model,

$$\begin{aligned} \partial_t q_1 + \delta_I^2 J(\psi_1, q_1) + \psi_{1x} &= \delta_M^3 \nabla^4 \psi_1 + w(y) \\ \partial_t q_2 + \delta_I^2 J(\psi_2, q_2) + \psi_{2x} &= \delta_M^3 \nabla^4 \psi_2, \end{aligned} \quad (3)$$

where ψ_1 and ψ_2 are the streamfunctions for the flow in the upper and lower layers and

The additional parameters that enter the two-layer model, λ and δ , are, respectively, the nondimensional inverse baroclinic deformation radius and the ratio of layer depths,

$$\lambda = \frac{L}{L_d}, \quad \delta = \frac{H_1}{H_2}, \quad L_d^2 = \frac{g'}{f^2} \frac{H_1 H_2}{H_1 + H_2},$$

where H_1 , H_2 , and g' are respectively the upper and lower layer depths and the reduced gravity at the layer interface. We define a Reynolds number for these models as the ratio δ^2/δ^3_M .

Most of our attention will be given to the case of a barotropic double gyre driven by an antisymmetric $w(y)$ of the form

$$w(y) = -\sin(\pi y) \quad (4)$$

over the domain $0 < x < 1$, $0 < y < 2$. This corresponds to a subtropical gyre in $0 < y < 1$ and a subpolar gyre in $1 < y < 2$. When the forcing is antisymmetric, the model admits solutions that possess a symmetry, $\psi(-y) = -\psi(y)$, as well as solutions that are nonsymmetric (asymmetric), for which $|\psi(-y)| \neq |\psi(y)|$. Because of this, we will often refer to the resulting model as a symmetric double-gyre model and distinguish between symmetric (meaning purely antisymmetric) and nonsymmetric solutions. Later in the paper, we will compare these symmetric barotropic double-gyre results with results from an asymmetric barotropic double-gyre model and a baroclinic double-gyre model.

The baroclinic double-gyre model is described by (3). Both it and the asymmetrically forced version of the barotropic double-gyre model are driven by a nonsymmetric Ekman suction.

$$w(y) = \begin{cases} -\sin(\pi y), & 0 < y \leq 1 \\ -r \sin(\pi y), & 1 < y < 2. \end{cases} \quad (5)$$

The parameter r is a constant. We will present barotropic results from the case $r = 0.9$ and baroclinic results for $r = 0.85$. Both of these make the cyclonic driving in the northern half-basin weaker than the anticyclonic driving in the southern half-basin.

In each of the models described above, a no-slip boundary condition is used on the sides of the basin.

3. Methods

We fix the value of the nondimensional inertial boundary layer thickness at $\delta_I = 0.04$ and concentrate on the dependence of the flow on the frictional boundary layer thickness, represented by the parameter δ_M . We will mainly work with δ_M in the range 0.02 to 0.04. Over this range, the ratio δ_I/δ_M increases from 1 to 2, and we move from a weakly nonlinear regime to what, by the standards of numerical models, is a strongly nonlinear regime. A measure of horizontal friction in the ocean is not well defined; however, 100–1000 $\text{m}^2 \text{s}^{-1}$ is a range of horizontal eddy diffusivities typically used in ocean models of moderate resolution. Taking $\beta = 2 \times 10^{-11} \text{m}^{-1} \text{s}^{-1}$, the corresponding range of values of δ_M^* is 17–37 km. If we use a horizontal scale of 1024 km for L_x , the corresponding range of δ_M is 0.017–0.037. We are therefore using values appropriate to a relatively narrow basin. This allows us to focus model resolution on the inertial recirculations that form near the western boundary. These will occupy a significant fraction of the zonal extent of the domain. One consequence of this decision is that the part of the domain occupied by the linear Sverdrup flow is relatively small. It is simplest to estimate oceanic values of δ_I^* by writing δ_I^* as $[(\text{curl})/(\rho_0 H \beta^2)]^{1/2}$ where “curl” is the magnitude of the wind stress curl. However, the choice of H in a barotropic model is not straightforward. Because horizontal scales tend to be larger in a barotropic model than in a baroclinic model, using the mean ocean depth for H results in a sluggish flow and underestimates the effects of nonlinearity. Instead, we use 500 m, comparable to the middepth of the thermocline along the axis of the Gulf Stream near 70°W. For values of the wind stress curl in the range 1×10^{-7} – $2 \times 10^{-7} \text{N m}^{-3}$ (cf. Milliff et al. 1996), this yields values of δ_I^* in the range 22–32 km. With 1024 km for L_x , δ_I becomes 0.022–0.032, slightly less than the value used here.

Our main focus is on aperiodic time-dependent solutions. However, we wish to examine the degree to which simpler

solutions of the flow equations influence the aperiodic behavior. We will therefore follow branches of solutions of the antisymmetrically forced barotropic problem that are steady equilibria and periodic oscillations. In doing so we exploit the symmetry of (2). Because the forcing in the barotropic double-gyre problem is purely antisymmetric, (2) can possess two types of solutions, those which are purely antisymmetric about $y = 1$ and those which are nonsymmetric. The antisymmetric solutions can be stabilized against nonsymmetric perturbations by the simple expedient of enforcing antisymmetry in the numerical code. We will therefore use two numerical models based on (2), one which enforces antisymmetry and one which makes no assumptions about symmetry. Both use standard numerical schemes to solve (2) on a square grid with uniform spacing (Roache 1972). Equation (2) is discretized on a 129×257 grid. An explicit time-stepping scheme is used for all terms in (2) (a second-order Runge–Kutta scheme). The Poisson problem is solved using Hockney’s FACR method (Hockney 1970).

A second consequence of the symmetry properties of (2), when forced antisymmetrically, is that nonsymmetric solutions, whether steady or time dependent, occur in pairs that are mirror images of each other under reflection in the line $y = 1$. Our main diagnostic variable will be the basin integral of the kinetic energy of the flow, $K(t)$. This is insensitive to reflection of the solution in $y = 1$ and so maps the two members of a mirror-image pair of nonsymmetric solutions to the same instantaneous numerical value of the diagnostic. When it is necessary to distinguish the symmetry of a nonsymmetric solution, we will also use a secondary diagnostic, the kinetic energy of the flow integrated over the southern half of the basin, $0 < x, y < 1$, which we will call $K_S(t)$. This pair of diagnostics provides a simple way of distinguishing antisymmetric solutions from nonsymmetric solutions since the former satisfy $K = 2K_S$.

Occasionally, we will use dimensional quantities to try and provide a physical feeling for some of the results. In particular, rather than reporting times in nondimensional units, we will use days to better convey a sense of the length of some of the timescales involved. To obtain dimensional quantities, we use $L = 1024$ km and $\beta = 2 \times 10^{-11} \text{ m}^{-1} \text{ s}^{-1}$, which yields a timescale of 4.88×10^4 s so that one nondimensional time unit corresponds to approximately 13.6 h.

4. Results

In this section we discuss results from three sets of experiments. In the first set, summarized in Fig. 1 (a), the barotropic double-gyre model is forced symmetrically, $r = 1$, and δ_M is varied over the range 0.04 to 0.024. In the second set, summarized in Fig. 17 (b), the barotropic double gyre model is forced asymmetrically, $r = 0.9$, and δ_M is varied from 0.035 to 0.028. From the third set, an asymmetrically forced baroclinic double-gyre model with $r = 0.85$, only one experiment is shown, with $\delta_M = 0.02$. For all of these runs, $\delta_I = 0.04$. For the baroclinic model, two further parameters must be specified: λ (0.039) and δ (1/9).

We encounter four basic types of solution classifiable by their time dependence: steady, periodic, toroidal, and aperiodic. Toroidal solutions are those that follow trajectories confined to a 2-torus in the phase space of the model. They include quasiperiodic solutions as well as those periodic solutions that correspond to phase-locked orbits on the torus. In principle, quasiperiodic solutions with more than two primary frequencies are possible but are unlikely to be stable; we found no solutions of this sort. The focus of our interest is the aperiodic solutions since these are a more realistic oceanic regime; however, to understand the form of the aperiodic solutions it is useful to first understand the simpler solutions.

a. Purely antisymmetric forcing, $r = 1$

A regime diagram summarizing some of the results obtained may be seen in Fig. 1 (a). This includes three families of fixed points, three families of periodic solutions, and a number of aperiodic solutions.

1) SIMPLE SOLUTIONS: STEADY STATES AND LIMIT CYCLES

The disposition of steady states is comparable to that found by CI at a similar value of δ_P , despite the difference in boundary conditions along the zonal boundaries. At large δ_M , the model exhibits a single steady solution, antisymmetric about the middle latitude of the basin. As δ_M decreases, additional steady states branch from this in pitchfork bifurcations. These new steady states are created in pairs with the members of the pair being mirror images of each other. In this model, we observed one such bifurcation that occurred near $\delta_M = 0.036$. The new steady states are nonsymmetric. Since they are mirror images under reflection in the midline of the domain, they have the same basin-integrated kinetic energy and hence show up as a single branch in the regime diagram, Fig. 1 (a). The nonsymmetric steady states have lower energy than the antisymmetric states, a result that can be rationalized as follows. In the antisymmetric states, the input of potential vorticity by the Ekman pumping can only be balanced by diffusive transports between the inertial recirculations and to the boundaries. As friction is decreased, the velocity gradients must increase to maintain the diffusive transports, so the strengths of the

recirculations increase. For the same diffusivity, in the nonsymmetric states, at least one of the inertial recirculations crosses the zero wind stress curl line (ZWCL). Potential vorticity is transported advectively across the ZWCL and some of the vorticity input by the wind on each side of the ZWCL is directly canceled by vorticity input from the wind on the other side of the ZWCL, reducing the need for diffusive transport and hence reducing the net energy of the circulation. Furthermore, in an asymmetric steady state, the boundary between the inertial recirculations is longer, so more diffusive transport can occur for a given average shear.

After the appearance of nonsymmetric steady states, the steady states on the antisymmetric branch are unstable. However, they remain stable in the antisymmetric version of the code, which allows us to follow the antisymmetric branch to smaller values of δ_M . We encounter a tangent bifurcation just below $\delta_M = 0.031$ at an energy of $O(140\ 000)$. A second tangent bifurcation involving antisymmetric solutions occurs at a higher energy, of $O(10^6)$, near $\delta_M = 0.032$. It is probable that the two tangent bifurcations are connected by antisymmetric states that are unstable to antisymmetric perturbations, as sketched with diamonds in [Fig. 2](#). This is consistent with the results reported by CI.

In [Fig. 3](#), we show examples of some of the steady states. [Figure 3a](#) shows the antisymmetric solution at $\delta_M = 0.04$. In both northern and southern halves of the domain, we see a western boundary current, a slow Sverdrup-like interior and an inertial recirculation near the intergyre boundary. [Figures 3b–d](#) are three of the steady states that exist at $\delta_M = 0.031$. At this value of δ_M we located two antisymmetric states, one at intermediate energy ([Fig. 3b](#)) and one at high energy ([Fig. 3c](#)). A third, strongly unstable, antisymmetric steady state probably exists at an energy between these two (cf. CI). There is also a pair of nonsymmetric states that are mirror images of each other and have lower energy than either of the antisymmetric states ([Fig. 3d](#)). Using the dimensional parameter set described in [section 3](#), the transport in the gyre in the intermediate energy antisymmetric solution is 22.8 Sv ($\text{Sv} \equiv 10^6 \text{ m}^3 \text{ s}^{-1}$) while in the high energy solution it is 79.4 Sv. The transport in the inertial gyres of the nonsymmetric solution is less than was the case for either of the antisymmetric solutions, being 13.7 Sv in the stronger gyre. There is a stagnation point on the western boundary that can be used to define where the two western boundary currents meet. The inertial gyre that belongs to the half-basin that contains this stagnation point is stronger than its counterpart in the other half-basin. The streamlines adjacent to the weaker inertial gyre, on the side opposite that which abuts the stronger gyre, have a pronounced Ω shape. In the example shown in [Fig. 3d](#), this lies to the south of the southern recirculation gyre, and the axis of the Ω runs SW–NE. Between the head of the Ω and the western boundary current there is a small, weak recirculation. There is also a weak recirculation on the side of the Ω farthest from the main inertial recirculations. Both of these secondary recirculations strengthen as δ_M is decreased further, as can be seen in [Fig. 3e](#), which shows the corresponding nonsymmetric solution when $\delta_M = 0.029$.

Both the nonsymmetric and the antisymmetric branches of solutions become unstable to oscillatory modes, which equilibrate at finite amplitude and give rise to limit cycle solutions. The Hopf bifurcation on the nonsymmetric branch occurs close to $\delta_M = 0.0314$ and appears to be supercritical. The ensuing limit cycles are, of course, nonsymmetric and they occur in mirror-image pairs. An example may be seen in [Fig. 4](#), which shows the limit cycle at $\delta_M = 0.0314$. This branch of limit cycles is initially stable and can be followed down to $\delta_M = 0.0295$. A little below this, the limit cycle loses stability, but there is no evidence that it does not continue as an unstable limit cycle to smaller values of δ_M . The period of the limit cycle close to the original Hopf bifurcation is 31.05 days. As δ_M is reduced, the period slowly increases, reaching 31.31 days at $\delta_M = 0.0295$.

The antisymmetric branch of solutions undergoes a Hopf bifurcation near $\delta_M = 0.0327$, giving rise to small amplitude limit cycles with a period close to 29.74 days. These limit cycles are themselves antisymmetric. They are unstable to nonsymmetric perturbations but at first they are stable to antisymmetric perturbations. This allows us to follow this branch of antisymmetric limit cycles to $\delta_M = 0.0295$ where they lose stability to antisymmetric perturbations. At this point the period of these limit cycles has decreased to 29.22 days. Once again, there is no evidence of a saddle-node bifurcation terminating this branch of limit cycles at $\delta_M = 0.0295$, thus we assume that the branch of unstable limit cycles continues to smaller δ_M .

A third branch of limit cycles can be found, starting near $\delta_M = 0.0293$. These are very high energy antisymmetric limit cycles. They are unstable to nonsymmetric perturbations. At $\delta_M = 0.0293$, this limit cycle has a period of 22.67 days. By $\delta_M = 0.0265$, the period has become 18.28 days. The source of this branch of limit cycles has not been ascertained. It is difficult to follow an unstable limit cycle in a dynamical system of this size. The two obvious possibilities are (i) that this high energy branch of limit cycles bifurcated directly from the branch of antisymmetric steady states, initially as a limit cycle that was unstable to antisymmetric disturbances but which later stabilized, or (ii) that this branch of limit cycles is connected

to the lower energy branch of antisymmetric limit cycles via a pair of saddle-node bifurcations so that the high and low energy branches of antisymmetric limit cycles form the upper and lower parts of an S-shaped curve and are connected by an unstable branch of antisymmetric limit cycles that forms the middle of the S. We believe that the second possibility is unlikely. Neither the low δ_M end of the lower energy branch nor the high δ_M end of the higher energy branch show any evidence of turning that would be consistent with an approach to a saddle-node bifurcation. Moreover, the periods of the limit cycles on the two branches are dissimilar.

The nonsymmetric limit cycles undergo a second Hopf bifurcation between $\delta_M = 0.029\ 423$ and $\delta_M = 0.029\ 369$. The new period introduced by this secondary instability of the limit cycle is approximately 285 days. However, at $\delta_M = 0.029\ 369$, the slowly growing instability does not equilibrate onto a small amplitude toroidal attractor. Instead the amplitude of the secondary oscillation grows large and the solution is captured by the aperiodic attractor, suggesting that this secondary Hopf bifurcation is subcritical. At larger values of δ_p , this secondary Hopf bifurcation becomes supercritical.

2) APERIODIC SOLUTIONS

At sufficiently small values of δ_M , aperiodic solutions can be found. Like the steady equilibria and the limit cycles, these too come in two flavors, antisymmetric and nonsymmetric. In practice, only the nonsymmetric solutions are attracting but unstable antisymmetric aperiodic solutions can be found using the antisymmetric version of the model. The average energies of a number of aperiodic solutions are marked in [Fig. 1](#). They appear to lie in a band that lies between the nonsymmetric limit cycles and the lower energy antisymmetric limit cycles. An interesting result of this study is the relation between the limit cycles and the aperiodic solutions. Before going on to discuss this, we note the richness of the solution space of this problem. Fixing δ_M and δ_p , one can find multiple solutions, both time dependent and steady. Which solution is observed depends on the constraints placed on the model (for example forcing it to preserve antisymmetry) and the choice of initial conditions. For example, near 0.0294, we have found three unstable steady equilibria, one antisymmetric and two nonsymmetric, two unstable antisymmetric limit cycles, two stable nonsymmetric limit cycles, one unstable antisymmetric aperiodic solution and one stable nonsymmetric aperiodic solution, that is, nine solutions, three of which are locally attracting. In addition it is possible that other unstable solutions, which we have not found, may exist.

We present segments of time series from several aperiodic runs in [Fig. 5](#). Each segment is 20 000 days long. [Figure 5a](#) shows a segment from a time series of K from a run with $\delta_M = 0.0307$. In [Figs. 5b–d](#), $\delta_M = 0.029$, $\delta_M = 0.028$, and $\delta_M = 0.024$, respectively. Each shows irregular fluctuations between low and high values of the kinetic energy. In these fluctuations, the maximum energy, the minimum energy, and the time taken for a complete low–high–low cycle all vary irregularly from one fluctuation to the next. The average period of the large amplitude fluctuations is 552 days for $\delta_M = 0.0307$, 447 days for $\delta_M = 0.029$, and 440 days for $\delta_M = 0.028$. Note that these timescales are distinct from the new period introduced by the secondary Hopf bifurcation near $\delta_M = 0.029\ 37$. Superimposed on these are smaller amplitude oscillations with much shorter periods comparable to those of the limit cycles described above. The time series in [Fig. 5](#) show a tendency for the solutions to linger near the high and low ends of these fluctuations, performing several of the rapid limit-cycle-like oscillations at each peak and trough of the large amplitude fluctuation. An example of this can be seen more clearly in a shorter segment of the time series of K from the $\delta_M = 0.029$ run, which may be seen in [Fig. 6](#). From [Fig. 5](#), it is clear that, on average, at the larger values of δ_M , more time is spent in the vicinity of the peaks of the large amplitude fluctuations than at the troughs and the time spent lingering near the peaks decreases with decreasing δ_M .

At the sides of the panels in [Figs. 5a and 5b](#), we have marked the values of the mean kinetic energy for the nonsymmetric fixed points (NFP), the nonsymmetric limit cycles (NLC), and the lowest energy symmetric limit cycle (SLC). The mean energies of both the nonsymmetric fixed point and the nonsymmetric limit cycles lie close to the troughs of the large amplitude vacillations, while the high-frequency oscillations in the largest peaks of these vacillations straddle the mean energies of the low energy symmetric limit cycles. At first sight, these observations are consistent with the conjecture, stated in the introduction, that the “simple” solutions of the circulation problem, the steady equilibria, and the limit cycles play a significant role in influencing the “complicated” aperiodic evolution of the circulation, even when the “simple” solutions are unstable. For example, [Fig. 5](#) suggests that the circulation is making large amplitude, low-frequency vacillations from the vicinity of the antisymmetric limit cycle to the vicinity of the nonsymmetric limit cycles and steady equilibria. We shall see later that the situation is more complicated than this.

Following the example of [McCalpin and Haidvogel \(1996\)](#), we generate a histogram of the kinetic energy time series and look for evidence of two modes that might reflect the tendency to linger near the high and low energy states of the large amplitude vacillation. To construct this, we take a 100 000 day segment of the kinetic energy time series $K(t)$, sample at 1-day intervals, determine the maximum and minimum of the sampled values of kinetic energy, split the range between them

into 400 bins of equal width, and then count the number of samples that fall within each bin. This frequency is plotted in [Fig. 7](#) for each of the four values of δ_M used in [Fig. 5](#). There is a relatively pronounced peak at a low energy value that corresponds to the fact that the large amplitude fluctuations have troughs of roughly the same value. In [Fig. 7a](#), there is a second peak at around 83 000. However, the peaks of the fluctuations tend to be spread over a range of values and the amplitude of the high-frequency limit cycle behavior that is often seen at the peaks is fairly large. These two factors prevent us from seeing any well-defined second mode at high energy values in [Figs. 7b–d](#). We can try to remove the second of these effects by taking a running mean of the time series and plotting a histogram from this running mean. The running mean $\langle K(t) \rangle$ is defined as

$$\langle K(t) \rangle = \int_{t-T}^t K(t') dt',$$

where T is taken to be equal to the period of the high-frequency oscillations. In [Fig. 8a](#), we show a 20 000-day segment from a time series of $\langle K(t) \rangle$ from a run with $\delta_M = 0.029$. In [Fig. 8b](#), we show a histogram of the values in the smoothed time series in [Fig. 8a](#). Comparing [Fig. 8b](#) to [Fig. 7b](#), there is some suggestion of a peak near an energy value of 120 000 in the histogram obtained from the smoothed time series but no indication of a strongly preferred high energy mode.

There is a pronounced difference between the variation in the values of the minima of the large amplitude fluctuations and the values of the maxima. For the case $\delta_M = 0.029$, virtually all of the minima lie within $\pm 10\%$ of 45 000. The scatter in the maxima is much larger; the value of the largest maximum seen in [Fig. 5b](#) is almost twice the value of the smallest maximum. The variations in the heights of the maxima are irregular and introduce low-frequency components to the variability of the time series. This low-frequency variability becomes prominent when one looks at a power spectrum of the $K(t)$ time series. In [Fig. 9](#), we show power spectra of time series from runs made with the four values of δ_M used in [Fig. 5](#). In [Fig. 9b](#), we see a prominent peak at a period of approximately 30.06 days and a smaller, but clear, peak at 28.09 days. The period of the first peak is close to that of the low energy antisymmetric limit cycle, while that of the second is close to that of the nonsymmetric limit cycle. The difference in the amplitude of the peaks is consistent with the idea that the time series lingers for longer times in the vicinity of the antisymmetric limit cycle when it is at the peaks of the large amplitude fluctuations and for shorter times in the vicinity of the nonsymmetric limit cycle when it is in the troughs of the large amplitude fluctuations. However, there is an alternative explanation of the peak at 28.09 days. Note that other spectral peaks can be seen at long periods near 431 days and 395 days. These correspond to the basic timescale of the large amplitude fluctuations themselves and agree fairly well with the timescale of these fluctuations estimated earlier by just counting the number of fluctuations in a 20 000 day period. At periods longer than these, we see substantial power at periods out to the longest resolved timescale (32 768 days). This power at timescales longer than $O(400)$ days is associated principally with the variation in the sizes of the extrema of the large amplitude fluctuations. It is possible that the 28.09-day peak is a cross-harmonic arising from an interaction between the dominant mesoscale peak at 30.06 days and the $O(400)$ day) vacillation.

As we progress to smaller values of δ_M , for example, $\delta_M = 0.024$ shown in [Figs. 5d](#) and [9d](#), the irregularity in the large amplitude fluctuations increases. The range of variation in the values of both the minima and the maxima of these fluctuations becomes much greater. There are episodic excursions to very high energy values and there is little visible tendency of the time series to linger near the very high peaks. From the panels in [Fig. 9](#), we see that, as δ_M decreases, there is a tendency for the spectrum to fill out at periods longer than the dominant timescale of the large amplitude fluctuations. By the time we reach $\delta_M = 0.024$ ([Fig. 9d](#)), the large amplitude fluctuations have become so irregular that there is no longer a clear spectral peak at a “dominant” timescale for the large amplitude fluctuations in K . Instead the power spectral amplitude shows a steep slope upward as one moves to longer periods once one is at a period longer than $O(100)$ days. This upward slope levels off at a timescale of $O(1000)$ days, and there is a plateau in spectral amplitude from this timescale out to the longest period resolved by the spectrum, 32 768 days.

The conjecture raised by [Fig. 5](#) is that the large amplitude irregular vacillation is a cycling between the neighborhood of the nonsymmetric limit cycles and the vicinity of the low energy antisymmetric limit cycle. We can further test this conjecture on the role played by the limit cycles by comparing the evolution of the aperiodic circulation in the vicinity of a peak or trough of the large amplitude vacillations in kinetic energy with the simpler solutions shown in the earlier figures. The panels of [Fig. 10](#) show snapshots of the circulation over a period when the solution is in the vicinity of one of the high energy peaks of the large amplitude vacillation for the run with $\delta_M = 0.029$. They are separated by intervals of roughly a quarter-period of the high-frequency oscillation. The circulation in [Fig. 10](#) is in a state close to antisymmetric, with large inertial recirculations, but the high-frequency oscillation about this state is asymmetric. In particular, the axis separating the two main recirculations cycles from a zonal to a NW–SE orientation and back to zonal but does not make an excursion in the opposite direction in this example. When the solution is near one of the energy minima of the large amplitude

vacillation, the inertial gyres are more compact and the circulation undergoes a nonsymmetric oscillation.

The run with the lowest value, $\delta_M = 0.024$, shows the least evidence for the influence of the low-energy antisymmetric limit cycle on the solution (Figs. 5d, 7d, and 9d). When the circulation is sampled at one of the high energy peaks, it is not visibly closer to an antisymmetric state (see Fig. 11a) than it is when the flow is sampled in one of the low energy troughs (Fig. 11b). The kinetic energy histogram, Fig. 7d, shows no peak other than one at the relatively well-defined average energy of the troughs of the large amplitude fluctuation. However, this is not indicative of any preference for one of the nonsymmetric limit cycles when the circulation is in a low energy state. In Fig. 11b, we see that the inertial gyres are much more compact than they were for the antisymmetric limit cycles and steady state (all of which, if the solution branches were extrapolated to this δ_M , would have higher energy than that corresponding to Fig. 11b). However, the disposition of the main recirculation gyres in Fig. 11b is close to antisymmetric and does not resemble the nonsymmetric steady states or limit cycles.

The cracks that have begun to appear in the edifice of our simple explanation of the large amplitude vacillations widen when we carefully examine the behavior of the aperiodic solution seen at $\delta_M = 0.0307$. This lies closer to the part of the parameter line (the δ_M axis) at which we first see aperiodic behavior, so the nature of its onset ought to be more apparent. In Fig. 12, we show a short segment of the basin-integrated kinetic energy time series from a much longer run. In Fig. 13, we show two snapshots spaced 16 days apart during a period that corresponds to the interval $452 \leq t \leq 468$ in Fig. 12. This is roughly one-half cycle of the fast oscillation period while the circulation is in one of the troughs of the large amplitude vacillation. In Fig. 14, we show two snapshots spaced 16 days apart during a second period that corresponds to the interval $800 \leq t \leq 816$. The main difference between the two intervals is the size of the main recirculation gyres. When the basin-integrated kinetic energy is low, the inertial gyres are small and the recirculating transport is weak. When the basin-integrated kinetic energy is high, the main inertial gyres are nearly twice as large in the zonal direction and the recirculating transport within them is roughly 50% larger. If we look at the behavior of the circulation in the trough, the dipole formed by inertial recirculation gyres oscillates around an approximately symmetric configuration in which the axis of the dipole is zonal and the strengths of the two gyres are equal and opposite. In the course of the roughly 30-day oscillation, the axis of the dipole nutates north and south slightly while the strengths of the two gyres wax and wane in antiphase. At the same time Rossby waves can be seen propagating westward in each half-basin. From the asymmetry between their zonal and meridional scales, one can deduce that the zonal component of their group velocity is eastward. These are therefore excited either at the western boundary or near the inertial recirculations.

The behavior of the circulation over the short oscillation period when the basin-integrated kinetic energy is near a peak of the slow vacillation is fundamentally different from the behavior near a trough. It possesses a definite asymmetry. During the short oscillation from which Fig. 14 is taken, the separation point on the western boundary, between the two main recirculation gyres, is located to the north of the midline of the basin throughout the cycle. The latitude of the separation point oscillates during this cycle. The axis between the two inertial gyres is tilted in the SW–NE direction throughout the oscillation though its direction goes through a cycle of being more or less inclined to the zonal direction during the oscillation. At one point during the cycle, this axial direction is almost zonal though the axis is still north of the midline of the basin. As in the low energy oscillation shown in Fig. 13, large amplitude Rossby waves with westward phase speed and eastward group velocity can be seen in each half-basin outside the inertial recirculation gyres. At some of the other peaks in the large amplitude vacillation cycle, the behavior of the circulation is similar to that just described. At the other peaks it is similar with the important difference that the asymmetry is reversed. The aperiodic solutions described here for this antisymmetrically forced problem randomly switch back and forth between a regime in which the latitude of the intergyre separation point is north of the midlatitude line and a regime in which it is south of this line. This type of aperiodic solution does not exhibit the division into a pair of solutions with mirror image symmetry that is seen for the simpler nonsymmetric solutions. Its average behavior is, in fact, symmetric. The results of this circulation problem therefore exhibit an interesting sequence: at low Reynolds number the preferred state is symmetric, at higher Reynolds number the attracting states are nonsymmetric, while at still higher Reynolds numbers the attracting state is an aperiodic solution that is, in general, instantaneously nonsymmetric but, on average, is symmetric.

Another way to bring out some of the structure of the aperiodic circulation is to project it onto a phase space of reduced dimension. We do that as follows. From the barotropic GCM described in section 2, we record two time series: one, $K(t)$, is the basin-integrated kinetic energy and the second, $K_S(t)$, is the kinetic energy of the flow integrated over the southern half of the basin only. From these we construct three phase coordinates:

$$\begin{aligned} X(t) &= K(t) - 2K_S(t), & Y(t) &= K(t), \\ Z(t) &= K(t - \tau), \end{aligned}$$

where τ is a fixed time delay, taken here to be seven days, that is, roughly a quarter of the period of the fundamental limit

cycles. [See [Meacham and Berloff \(1997\)](#) for a discussion of the sensitivity of delayed projections of phase space to the choice of delay.] With this choice, a purely antisymmetric solution lies in the plane $X = 0$. The results for $\delta_M = 0.0307$ and $\delta_M = 0.029$ are shown in [Fig. 15](#). In both parts of this figure, we show a trajectory corresponding to the aperiodic circulation and the adjacent simple solutions that we know of: the nonsymmetric steady equilibria, the nonsymmetric limit cycles, and the lower energy antisymmetric limit cycles. The antisymmetric fixed points and the higher energy antisymmetric limit cycles are far from the aperiodic trajectories and are not shown in [Fig. 15](#). In both [Figs. 15a and 15b](#), the aperiodic trajectories exhibit a rapid looping motion, associated with the high-frequency [$O(30 \text{ day})$ oscillation] and a slower, but much larger amplitude vacillation in a lobe in the left or right half plane. This switchover occurs at irregular intervals. The behavior of the aperiodic trajectory is sketched in [Fig. 16](#). Its large-scale behavior, that is, neglecting the rapid looping, is reminiscent of the behavior seen in the neighborhood of a homoclinic bifurcation (see [Sparrow 1982](#) or [Wiggins 1990](#)). The solution makes a series of large loops (with smaller mesoscale oscillations superimposed) in one or another of the semicardiod lobes, D and D' in [Fig. 16](#). At the end of each loop, the solution returns to a region, G , surrounding a point of relatively low energy on the symmetry plane. Sometimes the solution is ejected out of region G in the same half-space as it entered ($X > 0$ or $X < 0$), and sometimes it crosses the symmetry plane while in G and leaves in the opposite half-space. In doing so, it switches between favoring the subtropical gyre and the subpolar gyre. However, if the hypothesis that this type of attractor appears as a result of a homoclinic bifurcation (strictly speaking, a pair of simultaneous homoclinic bifurcations, thanks to the antisymmetry of the problem) is correct, then there should be a simple hyperbolic solution, such as an unstable fixed point or limit cycle located in the region marked G on [Fig. 16](#). We have been unable to find such a solution, though our methods for finding such a solution are rudimentary. If the hyperbolic solution were a single fixed point, then one would expect it to be an antisymmetric steady equilibrium flow lying on the plane $X = 0$. One would also expect a chaotic time series of long duration associated with a trajectory close to this homoclinic tangle to show occasional intervals when the trajectory, having come close to this equilibrium point, lingers there, moving slowly for an extended time. We do not see evidence of this. Instead, when the aperiodic trajectory is in the low energy part of its large amplitude vacillation, we see, as noted above, a limit-cycle-like oscillation of finite amplitude. This limit cycle appears to be about an antisymmetric state but is not itself antisymmetric. If we are close to a homoclinic bifurcation, then it seems more plausible that the hyperbolic object that undergoes this bifurcation is a limit cycle, and a limit cycle that does not correspond to one of the families of limit cycles discussed earlier. From the form of the oscillation seen in [Fig. 14](#), we are led to speculate that this limit cycle arises through an instability of the dipolar structure formed by the pair of inertial recirculation gyres. However, since there is no antisymmetric steady equilibrium at this low an energy, such a limit cycle, if it exists, must either arise through a saddle-node bifurcation or bifurcate from a now distant steady state. Since we are unable to isolate this limit cycle, we have not been able to determine the physical mechanism responsible for its origin. However, our results suggest an important role for such a mechanism in the low-frequency variability of the barotropic double-gyre wind-driven circulation.

The origin of the irregular low-frequency vacillation in a homoclinic bifurcation, rather than a secondary Hopf bifurcation, demonstrates that it is quite unlike either the toroidal solutions with low-frequency components seen in the baroclinic single-gyre problems considered by [Holland and Haidvogel \(1981\)](#) and [Berloff and Meacham \(1998\)](#) or the vacillation of the amplitude of a baroclinic instability in a weakly unstable zonal channel flow described by [Pedlosky \(1970\)](#).

Rather than temporarily attracting the aperiodic solutions, some of the simple solutions appear to act as barriers, confining the aperiodic solution in phase space. The lower energy example of the two antisymmetric limit cycle solutions lies between the two semicardiod lobes in [Fig. 15](#), near the high energy limit of the aperiodic trajectories. Occasionally, when $\delta_M = 0.029$, the aperiodic trajectory approaches the antisymmetric limit cycle but most of the time the aperiodic trajectory is not strongly attracted by the antisymmetric limit cycle.

As δ_M is reduced further, increasing the nonlinearity of the flow, we see the volume of phase space occupied by the aperiodic trajectory increase slightly. It appears to press close to the unstable nonsymmetric limit cycles, though it does not linger in their vicinity, and make occasional excursions through these limit cycles to the neighborhoods of the fixed points that are the nonsymmetric steady-state solutions.

However, the two nonsymmetric limit cycles and the low energy antisymmetric limit cycle appear to bound the region of phase space occupied by the aperiodic solution.

If we take the aperiodic solution starting at $\delta_M = 0.0307$ and gradually increase δ_M , each time initializing the model with a snapshot of the aperiodic solution from the previous δ_M , we find that between $\delta_M = 0.03076$ and $\delta_M = 0.03084$ the aperiodic solution loses stability and the solution is captured by one of the nonsymmetric limit cycles. The aperiodic solution does not show any particular limiting structure as one approaches the δ_M where stability is lost, suggesting that the irregular, aperiodic solution undergoes a saddle-node bifurcation. Thus, the irregular aperiodic attractor probably arises either through a subcritical bifurcation from some simpler stable solution or as a bifurcation to an unstable solution from a simpler unstable solution. Since, close to this bifurcation, the newly bifurcated solution is unstable, we cannot easily identify the instability

that gives rise to the aperiodic behavior that is, in turn, associated with low-frequency variability. The form of the aperiodic trajectories suggests the existence of a homoclinic bifurcation but the numerical evidence suggests that this is a subcritical bifurcation, which makes it difficult to explore the details of the bifurcation.

In none of the situations where we find aperiodic behavior, even the case closest to the loss of stability of the aperiodic solution, do we see an aperiodic solution that lies only in one of the half-spaces $X > 0$ or $X < 0$. In all cases, the aperiodic trajectories, over a long time interval, spend similar amounts of time in both half-spaces.

Setting aside the question of the origin of the low energy limit cycle noted above, the structure seen in [Fig. 15](#) and sketched in [Fig. 16](#) provides some important clues to the physics behind the low-frequency vacillation. We present a hypothesis to explain this vacillation as part of the discussion in [section 5](#).

b. Asymmetrically forced barotropic double gyre

The symmetric barotropic model driven by a purely antisymmetric Ekman suction may seem something of a special case. We have therefore gone on to explore the behavior of a barotropic double-gyre model driven by an asymmetric Ekman suction of the form [\(5\)](#) for several values of r . We report here some results for the case $r = 0.9$. When the forcing is asymmetric, it is no longer possible to restrict the model and artificially stabilize the counterparts of the unstable antisymmetric solutions seen in the symmetric problem. However, we are able to demonstrate both a saddle-node bifurcation corresponding to the pitchfork bifurcation in the symmetric problem that gave rise to the pair of asymmetric solutions and a pair of Hopf bifurcations corresponding to the Hopf bifurcations of the nonsymmetric steady states in the symmetric problem. This is summarized in the crude bifurcation diagram in [Fig. 17](#). At high δ_M , there is a single attractor, a steady state. Its counterpart in the symmetric problem is the single branch of antisymmetric steady states seen at high δ_M . Near, 0.0334, we see a saddle-node bifurcation that gives rise to two more branches of solutions. One, shown in [Fig. 18](#), is a branch of stable steady states—the upper set of diamonds between 0.0334 and 0.031 in the figure. The second is a branch of unstable steady states that we have not followed. The counterparts of the stable branches, below $\delta_M = 0.0334$, are the two arms of the pitchfork bifurcation in the symmetric problem that correspond to nonsymmetric steady states. The counterpart of the unstable branch is the unstable continuation of the antisymmetric steady states at δ_M below the primary pitchfork bifurcation in the symmetric problem. Of the two branches of stable steady states, the lower energy branch has a more energetic flow in the southern half-basin than in the northern half-basin, while the opposite is true for the higher energy branch.

As δ_M is decreased, both of the branches of stable steady states undergo Hopf bifurcations, and we find two branches of stable limit cycles. Again, one branch has, when an average is taken over the period of the limit cycle, a southern half-basin with a higher kinetic energy than the northern half-basin, while the opposite is true for the second branch of limit cycles. Both of these branches of periodic solutions appear to undergo secondary Hopf bifurcations to produce stable toroidal attractors. At higher Reynolds numbers (lower δ_M), we encounter aperiodic solutions. A segment of a time series from an integration of length 94 000 days for the case $r = 0.9$, $\delta_I = 0.04$, $\delta_M = 0.029$ is shown in [Fig. 18](#). Note the similarity in form to [Figs. 5b and 5c](#) for the case $r = 1.0$, $\delta_I = 0.04$. In particular, we see an irregular large amplitude vacillation with a superimposed fast oscillation. The timescales of both the fast and the slow oscillations are similar to those observed in the antisymmetric problem. This is confirmed by the similarity between the power spectrum of the basin-integrated kinetic energy in the $r = 0.9$ case, [Fig. 19](#), and in the $r = 1.0$ cases, [Figs. 9a–c](#).

Using the same phase space variables as before, we can produce artificial phase space plots of the trajectories that correspond to the evolution of the circulation. When $\delta_M = 0.029$, we find that there are two stable regimes. The first is a toroidal attractor; the second is an aperiodic attractor. A segment of the time series $K(t)$ from the aperiodic solution may be seen in [Fig. 18](#), and the phase space projection of this aperiodic trajectory is shown in [Fig. 20](#). Unlike the aperiodic trajectories from the symmetric problem seen in [Fig. 15](#), the aperiodic trajectory fills out a single lobe rather than two. This lobe lies predominantly in the half-space $X < 0$ in which the circulation in the southern half-basin is stronger than that of the northern half-basin, an asymmetry that matches that of the wind stress curl. Along this trajectory, the more strongly forced southern half-basin nearly always has more energy than the northern half-basin. The toroidal attractor is also one on which the energy of the northern half-basin is less than that of the southern half-basin. At this value of $\delta_M = 0.029$, solutions that favor a stronger southern half-basin form the only attractors. This represents a range of δ_M where the behavior of the asymmetrically forced flow is distinctly different from that of the antisymmetrically forced flow. In the antisymmetrically forced problem at high δ_M , asymmetric solutions exist in pairs, one favoring one half-basin; the other favoring the second. At lower δ_M we saw aperiodic solutions that flipped backward and forward from favoring one half-basin to favoring the other. In this asymmetrically forced problem, at higher values of δ_M , there are attractors that prefer

either half-basin, just as in the antisymmetrically forced case. At $\delta_M = 0.029$, we can find no attractors that favor the more weakly forced half-basin. At still lower values of δ_M , we find aperiodic solutions that, while predominantly being in a state in which the southern half-basin has more energy than the northern half-basin, occasionally flip over so that the northern half-basin is the stronger. As δ_M decreases, the fraction of time for which the circulation in the northern half-basin is stronger than that in the southern half-basin increases.

c. A baroclinic model


One of the defects of a purely barotropic model is that, while it represents the vertically integrated transport driven by the wind, at least provided that the horizontal flow is sufficiently weak at the lower boundary that the effects of horizontally varying topography can be neglected, it does not model the vertical structure well. In particular, it omits a process believed to be an important source of time dependence for the general circulation, namely, baroclinic instability. We present here an example of a baroclinic double-gyre flow in order to demonstrate some notable similarities to the aperiodic barotropic solutions discussed above.




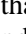
We use the two-layer quasigeostrophic model discussed in [section 2](#) and described by (3). The horizontal discretization and resolution is the same as that used for the barotropic model. We again set $\delta_l = 0.04$. We use a layer depth ratio of 0.111 and a baroclinic deformation radius that is 0.039 when scaled by the basin width. However, rather than using an antisymmetric Ekman suction field, we use a $w(y)$ of the form

$$w(y) = \begin{cases} -\sin(\pi y), & 0 < y \leq 1 \\ -r \sin(\pi y), & 1 < y < 2 \end{cases}$$

and set the parameter r to be 0.85. This means that the subtropical gyre in the southern half of the basin is driven somewhat more strongly than the subpolar gyre in the northern half of the basin.

When frictional processes are represented by a horizontal diffusion of momentum and no-slip boundary conditions are used, then the steady states of the two-layer model are isomorphic to those of the appropriate asymmetric barotropic model. They simply take the form of a lower layer at rest and an upper-layer flow that is an exact steady state of the barotropic problem with the same depth as that of the upper layer. In particular, the steady equilibria, while baroclinic, are independent of the baroclinic deformation radius. (Their stability to time-dependent perturbations is, of course, dependent on the baroclinic deformation radius.) The time-dependent solutions of the baroclinic problem are not going to be the same as those of the barotropic problem. Nevertheless, we shall see that there is some structural similarity between the aperiodic baroclinic and barotropic solutions.

The two-layer model takes longer to integrate than the barotropic model, but more daunting is that the timescale on which the baroclinic model converges to a simple solution such as a steady state or a periodic oscillation is much longer than was the case in the barotropic solution. This is to be expected since in the barotropic case the adjustment to a steady or time-dependent “equilibrium” circulation is mediated by relatively rapid barotropic Rossby waves, whereas in the baroclinic adjustment problem, the timescale for the equilibration of the layer interface is set by the much slower baroclinic Rossby waves. This long adjustment timescale makes the task of tracking branches of limit cycles prohibitively expensive, and we have not done this. Instead, we have made a few long simulations of aperiodic baroclinic solutions. We show here a run made with $\delta_M = 0.02$. In [Fig. 21](#) , we show a 100 000-day segment of a time series of upper-layer kinetic energy integrated over the southern half of the basin. As in the barotropic problem, there is an irregular, large amplitude fluctuation in energy on a long timescale. The troughs of these fluctuations lie in a relatively well-defined band of energies spanning the range 150–250 with a few exceptions. (The units of energy have been nondimensionalized and are not directly comparable to the nondimensional units used in the barotropic problem discussed in previous sections.) There is slightly more scatter in the values of the peaks of the fluctuations. Visually there seems to be a distinct timescale for these fluctuations, although the time between successive peaks or successive troughs is clearly variable. Counting the peaks we estimate 23½ large amplitude “cycles” in the 100 000-day interval suggesting a crude timescale estimate of 4255 days or roughly 11.65 years.

[Figure 22](#)  shows a series of random snapshots of the upper-layer streamfunction during the evolution of the circulation. We see that the flow fluctuates between quite different states. In [Fig. 22c](#)  the circulation is relatively “antisymmetric” in that a straight separation jet penetrates a substantial distance into the interior of the basin. Since the wind forcing is asymmetric, we do not expect to see a truly antisymmetric state but, if we compare the high and low energy extremes of the fluctuations seen in [Fig. 11](#)  or the difference in structure between the nonsymmetric and antisymmetric states shown in [Fig. 3](#) , we see that the higher energy states are characterized by a much greater eastward penetration of the jet that forms the common boundary between the two main inertial recirculations. In contrast, at a time like that shown

in [Fig. 22a](#), the flow is much more asymmetric, the inertial recirculations are more compact, and the separation jet is nonzonal, features shared by the nonsymmetric steady states in [Fig. 3](#). This is reinforced if we plot the instantaneous circulation seen near an energy maximum in [Fig. 21](#), shown in [Fig. 23a](#), and compare it with a plot of the streamfunction near an energy minimum, shown in [Fig. 23b](#). The differences in structure between high and low energy states are similar to those seen in [McCalpin and Haidvogel \(1996\)](#). However, the story in the baroclinic problem is more complicated than this. Some of the low energy states are associated with a type of flow that does not have a counterpart in the barotropic double-gyre problem, a circulation pattern in which the two main gyres have pulled apart leaving a band of relatively sluggish flow between them. An example of this is shown in [Fig. 24](#). This type of flow is reminiscent of episodes in the South Atlantic when the Brazil and Malvinas Currents separate at different latitudes and a zonal band of more sluggish water appears between them. Such events have been seen in satellite observations ([Olson et al. 1988](#)) and in hydrographic observations ([Roden 1986](#)). A potential mechanism is discussed in [Haidvogel et al. \(1992\)](#). In a study of boundary current separation in a QG baroclinic double gyre model, [Haidvogel et al. \(1992\)](#) diagnosed the time average of the ageostrophic part of the pressure gradient along the western wall and noted that, in cases where the western boundary currents separated before meeting each other, there was a strong adverse ageostrophic pressure gradient along the wall at the separation point. Near the boundary this balances the Coriolis acceleration associated with the offshore flow at the separation point. The mechanism determining the location of the separation points remains unclear.

Rather than present a detailed analysis of the complicated structure of this baroclinic circulation, we wish to emphasize the nature of the time dependence of this flow. If we compute a power spectrum of the kinetic energy of the upper-layer flow integrated over the southern half of the basin, as shown in [Fig. 25](#), we see that, while there are local spectral peaks at mesoscale timescales in the range 30 to 60 days, the dominant spectral peak occurs at a period of between 4096 and 4681 days. This corresponds to the timescale of the large amplitude fluctuations visible in [Fig. 21](#). The maximum eastward zonal group velocity of a plane baroclinic Rossby wave with no meridional variation is $\beta L_d^2/8$, where L_d is the baroclinic deformation radius. The time for this wave to cross a basin of width L is then $8/[(\beta L)(L_d/L)^2]$. Using a basin width of $L = 1024$ km, this becomes roughly 8.1 years. Adding a meridional wavenumber to the Rossby wave will reduce the zonal component of the group velocity still further. It therefore seems plausible that the low-frequency fluctuation seen in [Fig. 21](#) is associated with baroclinic vacillations in the structure of the wind-driven gyres.


5. Discussion


The results of this paper corroborate the results of earlier works, such as [Cox \(1987\)](#) and [Moro \(1990\)](#), who found evidence for naturally occurring low-frequency variability in the wind-driven circulation. In both the barotropic and baroclinic double-gyre problems, the amplitude of this low-frequency variability is very high. Physically, it is associated with large fluctuations in the strength and size of the inertial recirculation gyres. In the baroclinic problem, the vacillations in circulation energy are also associated with vacillations in the degree of mesoscale meandering of the intergyre jet. The existence and nature of low-frequency variability is robust to variations in symmetry of the steady wind forcing.




In the baroclinic problem, the dominant timescale associated with the low-frequency variability is decadal. Given the importance of the subtropical wind-driven gyres in meridional heat transport and the role of the position of the separated Gulf Stream and Kuroshio in fixing the locations of the regions of strongest ocean-to-atmosphere heat transfer, such variability on a decadal timescale will have a significant effect on the extratropical climate as a whole on decadal timescales.







The results also invalidate the hypothesis outlined in the introduction. The low-frequency variability seen in the barotropic double gyre model is not associated with peregrinations between several unstable states. The aperiodic trajectory in [Fig. 15](#) does not show signs of being transiently attracted to the unstable, nonsymmetric steady states or limit cycles nor to the unstable antisymmetric steady states and limit cycles identified in [Fig. 2](#). Instead, it appears to arise through a homoclinic bifurcation from a simpler state not found in the bifurcation analysis shown in [Fig. 2](#).



Before describing the physical processes behind the low-frequency vacillation, it is useful to compare the origins of low-frequency variability in the double-gyre models discussed here and in the single-gyre models examined by [Holland and Haidvogel \(1981\)](#), [Meacham and Berloff \(1997\)](#), and [Berloff and Meacham \(1998\)](#). In the latter two, the appearance of low-frequency variability was associated with the appearance of a chaotic attractor. A sequence of Hopf bifurcations led to the appearance of a strange attractor that, in the part of parameter space close to the onset of the strange attractor, resembled those seen in low-dimensional maps. The onset of the strange attractor resembles the loss of stability of a two- or three-frequency torus (cf. [Gollub and Benson 1980](#); [Giberti and Zanasi 1993](#); [Bak et al. 1985](#)). The amplitude of variability at long timescales is initially weak, just after the onset of the chaotic attractor, and it gradually increases as the Reynolds number is increased. In the double-gyre problem, the origin of low-frequency variability is somewhat different. While secondary Hopf bifurcations exist and introduce long timescales, the appearance of low-frequency variability is associated with what looks like a subcritical homoclinic bifurcation (a pair of simultaneous subcritical homoclinic bifurcations in the antisymmetric problem). [A standard example of a homoclinic bifurcation occurs in the Lorenz system ([Sparrow 1982](#)).] One consequence of this is that when low-frequency variability first appears, it appears with large amplitude. In basin-integrated statistics, the

low-frequency variations dwarf those due to mesoscale variability. Since the bifurcation is subcritical, there is no tendency for the dominant low-frequency timescale to become infinite as δ_M is increased toward the point where low-frequency variability disappears, as one would expect in a supercritical homoclinic bifurcation. In fact, near the onset of low-frequency variability, there is a rather pronounced dominant timescale for the variability and, only as δ_M is decreased further, does significant power appear in a broad range of low frequencies (see [Fig. 9d](#) ) .

It is possible that in a different range of δ_p , the homoclinic bifurcation may become supercritical. If such a range could be identified, it would simplify the task of determining the simpler solutions involved in the homoclinic bifurcation and hence the underlying physical mechanism. However, a diagnostic study of the low-frequency variations seen in [Fig. 5a](#)  provides some clues to the physical mechanism that supports them.

In the description that follows, it is useful to keep in mind a three-dimensional cartoon, with axes (X, Y, Z) , of the high-dimensional phase space of the double-gyre model, something like the three-dimensional projections shown in [Figs. 15](#)  and [16](#)  . In this cartoon, we distinguish the subspace of antisymmetric solutions (stationary or time dependent) and represent it by the plane $X = 0$. The X axis is then used to represent departures from antisymmetry. Distance from the origin in this cartoon should be thought of as being indicative of the energy of the flow. Consider the balances responsible for maintaining an antisymmetric steady state. In the cores of the inertial recirculations, the flow is approximately parallel to the closed contours of potential vorticity, the divergence of the advective transport of potential vorticity is weak, and the direct input of vorticity by the Ekman pumping is balanced by a combination of diffusive and advective transport. At low Reynolds numbers, this vorticity balance in the antisymmetric state is achieved at relatively low circulation energy but, as the eddy diffusivity of the flow is reduced, the location of the lowest energy antisymmetric steady solution moves to higher energies ([Fig. 2](#) ): the strengths of the inertial gyres increase so that the diffusive fluxes of vorticity necessary to balance the wind input of vorticity (which is unchanged) can be maintained despite the lowering of the eddy diffusivity. Above a critical Reynolds number, the antisymmetric steady states become unstable to nonsymmetric perturbations. Physically, this is easy to understand. Suppose the antisymmetric steady state is perturbed so that one of the inertial recirculations becomes slightly stronger than the other. The stronger recirculation will try to advect the weaker one around it so that the eastern end of the weaker recirculation crosses the zero wind stress curl line. The weaker gyre is now exposed to an Ekman pumping that is injecting potential vorticity with the opposite sign to the potential vorticity in the recirculation. This further weakens the weaker recirculation relative to the other inertial recirculation so that the weaker recirculation becomes even more distorted by the stronger recirculation. The antisymmetric steady state is now repelling in at least two of the directions (two, by symmetry) that correspond to nonsymmetric perturbations. Note that this instability cannot be thought of as a simple mesoscale instability, it is a large-scale instability of the (barotropic) inertial recirculations. The physical argument behind this loss of stability can be applied equally well to time-dependent antisymmetric states with strong inertial recirculations so that one expects that, for any given value of the extrinsic Reynolds number, trajectories in the part of the antisymmetric subspace that lies close to the origin of phase space (the low-energy solutions) will be stable to small nonsymmetric perturbations. As one moves farther away from the origin, the antisymmetric trajectories at sufficiently high energy will be unstable to nonsymmetric disturbances due to the physical mechanism just outlined.

At an extrinsic Reynolds number higher than, but close to, that of the homoclinic bifurcation, consider a phase of the vacillation cycle shown in [Fig. 16](#)  in which the overall energy of the flow is low and the flow is approximately antisymmetric (a point in the box G in [Fig. 16](#) ). At this low energy, the antisymmetric subspace is not strongly unstable and the solution will remain close to it. Since there are closed potential vorticity contours in the core of the inertial recirculations, vorticity pumped in by the wind stress curl accumulates in the recirculations. The flow is too weak for diffusion of vorticity to balance this input, so the recirculations increase in size (the slow march to higher energy parallel to the antisymmetry plane in [Fig. 16](#) ). Mesoscale variability is present but weak (and nonsymmetric). Eventually the approximately antisymmetric flow becomes so strong that the weak asymmetry present triggers the growth of the large-scale nonsymmetric instability in which one recirculation weakens while the other becomes stronger and distorts the shape of the weaker recirculation. This phase corresponds to the movement of the trajectory away from the antisymmetry plane along the upper edge of the butterfly wing in [Fig. 16](#)  . While the flow becomes increasingly nonsymmetric, the strong recirculation gyre continues to receive vorticity from the wind, becoming even stronger until eventually it becomes unstable to mesoscale instabilities. The amplitude of the mesoscale eddies in the the flow rapidly increases, the strong recirculation breaks up, and the overall energy of the flow rapidly decreases. The increase in mesoscale activity can be seen in [Fig. 16](#)  as an increase in the radius of the loops in the rapid looping motion that corresponds to mesoscale variability when the trajectory approaches the symbols D or D' . The drop in energy of the flow corresponds to the path of the trajectory back towards G in [Fig. 16](#)  . As the energy of the flow falls, it passes into the region of phase space near the origin in which motion on the antisymmetric subspace is attracting, and the flow becomes both low energy and approximately antisymmetric once again so that the cycle can repeat.

The large amplitude vacillation associated with the cycle just described is asymmetric in two senses. The energy of the flow increases more slowly than it decreases, as is clear in [Fig. 12](#)  . (This can also be deduced from [Fig. 16](#)  by noting that the diamond symbols are equally spaced in time.) In addition, the physical process by which the energy of the circulation increases is different from that responsible for the decrease. In the phase in which energy increases, the flow is

approximately antisymmetric, the energy and vorticity associated with the growth of the inertial recirculations are supplied by the wind and mesoscale variability is secondary. In contrast, in the phase in which energy is decreasing, the flow is significantly asymmetric and strong mesoscale eddies are present, mixing the potential vorticity field, and enhancing the level of dissipation. One candidate for the timescale that characterizes the decrease in the energy of the flow should therefore be the dissipative timescale associated with mesoscale eddies. If we crudely estimate this as L_e^2/ν , where L_e is an eddy length scale, and approximate L_e by δ_I , then this timescale can be written as $(\delta_I^2/\delta_M^3)(\beta L)^{-1}$ [$(\beta L)^{-1}$ was the timescale used to nondimensionalize (1)]. For $\beta = 2 \times 10^{-11} \text{ m}^{-1} \text{ s}^{-1}$, $L = 1024 \text{ km}$, $\delta_I = 0.04$, and $\delta_M = 0.03$, this scale is approximately 45 days. In Fig. 12, the timescale for the decay phase of the large amplitude vacillation is 90–120 days. A candidate for the timescale of the increase in energy of the vacillation can be obtained by considering an upper bound on the the barotropic adjustment timescale of the inertial recirculations, estimated as the transit time for a barotropic Rossby wave with a wavelength comparable to the short scale δ_I , that is, $0.5L/(\beta\delta_I^2) = \delta_I^{-2}(\beta L)^{-1}$. This is approximately 350 days. Another “annual” timescale can be obtained by taking the magnitude of the potential vorticity in the core of the recirculation gyres in the high energy, almost antisymmetric, phase (roughly $1 \times 10^{-5} \text{ s}^{-1}$) and dividing it by the rate of input of potential vorticity by the Ekman pumping/suction averaged over the area of the recirculation (roughly $0.45 \times 10^{-12} \text{ s}^{-2}$). The resulting timescale, approximately 260 days, is comparable to the $O(300 \text{ day})$ timescale of the increasing phase of the vacillations shown in Fig. 12. However, this is not a very plausible estimate for the following reasons. When the flow is in a steady state, there is a balance between (i) the potential vorticity input directly to the recirculations by the wind, (ii) potential vorticity input over the remainder of the gyre and collected by the western boundary currents, part of which is entrained into the recirculations from the separated intergyre jet, and (iii) the diffusion of potential vorticity between the recirculations. In the slow vacillations, the growth of the recirculations is determined by the imbalance between these three, of which (ii) and (iii) are larger than (i). This suggests that the $O(300 \text{ day})$ timescale that comes from just considering the direct wind input is a coincidence.

The vacillations seen in the numerical results and the physical mechanism outlined above should be viewed as an illustration of an oscillation mechanism that may be active in the ocean, just as the linear theory of Rossby waves describes another oscillation mechanism. In a more realistic setting, neither type of theory provides a detailed description of the complex nonlinear flow but the simple oscillation mechanisms can still provide insight into the dynamics of the flow.

This investigation provides an example of the potential of nonlinear interactions in the wind-driven ocean circulation to generate extremely long timescales. This seems a topic worthy of considerable research effort, not only for its own sake but because, on purely mathematical grounds, more complex ocean circulation models and coupled ocean–atmosphere models ought to exhibit similar behavior, albeit with different timescales and parameter dependence. Until the origin and nature of natural low-frequency variability, together with its dependence on the physical parameters of the ocean or climate system, are properly understood, decadal and longer timescale predictions will always contain a high degree of uncertainty.

Acknowledgments

The support of the National Science Foundation under the Contract OCE-9301318 is gratefully acknowledged. The author thanks Paola Cessi for several interesting discussions on this topic. It is with gratitude that the author acknowledges the support and continued friendship of a splendid colleague, Prof. Bill Dewar.

REFERENCES

- Bak, P., T. Bohr, and M. H. Jensen, 1985: Mode-locking and the transition to chaos in dissipative systems. *Physica Scripta*, **T9**, 50–58.
- Berloff, P. S., and S. P. Meacham, 1998: The dynamics of a simple baroclinic model of the wind-driven circulation. *J. Phys. Oceanogr.*, **28**, 361–388. [Find this article online](#)
- Bryan, K., 1963: A numerical investigation of a nonlinear model of a wind-driven ocean. *J. Atmos. Sci.*, **20**, 594–606. [Find this article online](#)
- Cessi, P., and G. R. Ierley, 1995: Symmetry-breaking multiple equilibria in quasigeostrophic wind-driven flows. *J. Phys. Oceanogr.*, **25**, 1196–1205. [Find this article online](#)
- Cox, M. D., 1987: An eddy-resolving model of the ventilated thermocline: Time dependence. *J. Phys. Oceanogr.*, **17**, 1044–1056. [Find this article online](#)
- Dijkstra, H. A., and C. A. Katsman, 1997: Temporal variability of the wind-driven quasi-geostrophic double gyre ocean circulation: Basic

Giberti, C., and R. Zanasi, 1993: Behavior of a three-torus in truncated Navier–Stokes equations. *Physica D*, **65**, 300–312..

Glendinning, P., 1994: *Stability, Instability and Chaos: An Introduction to the Theory of Nonlinear Differential Equations*. Cambridge University Press, 388 pp..

Gollub, J., and S. Benson, 1980: Many routes to turbulent convection. *J. Fluid Mech.*, **100**, 449–470..

Griffiths, R. W., and G. Veronis, 1997: A laboratory study of the effects of a sloping side boundary on wind-driven circulation in a homogeneous ocean model. *J. Mar. Res.*, **55**, 1103–1126..

Guckenheimer, J., and P. Holmes, 1983: *Nonlinear Oscillations, Dynamical Systems, and Bifurcations of Vector Fields*. Springer-Verlag, 453 pp..

Haidvogel, D. B., J. C. McWilliams, and P. R. Gent, 1992: Boundary current separation in a quasigeostrophic, eddy-resolving ocean circulation model. *J. Phys. Oceanogr.*, **22**, 882–902.. [Find this article online](#)

Hansen, D. V., and H. F. Bezdek, 1996: On the nature of decadal anomalies in North Atlantic sea surface temperature. *J. Geophys. Res.*, **101**, 8749–8758..

Hockney, R., 1970: The potential calculation and some applications. *Meth. Comput. Phys.*, **9**, 136–211..

Holland, W. R., 1978: The role of mesoscale eddies in the general circulation of the ocean: Numerical experiments using a wind-driven quasigeostrophic model. *J. Phys. Oceanogr.*, **8**, 363–392.. [Find this article online](#)

—, and L. B. Lin, 1975a: On the generation of mesoscale eddies and their contribution to the oceanic general circulation. I. A preliminary numerical experiment. *J. Phys. Oceanogr.*, **5**, 642–657.. [Find this article online](#)

—, and —, 1975b: On the generation of mesoscale eddies and their contribution to the oceanic general circulation. II. A parameter study. *J. Phys. Oceanogr.*, **5**, 658–669.. [Find this article online](#)

—, and D. B. Haidvogel, 1981: On the vacillation of an unstable baroclinic wave field in an eddy resolving model of the oceanic general circulation. *J. Phys. Oceanogr.*, **11**, 557–568.. [Find this article online](#)

Hurrell, J. W., 1996: Influence of variations in extratropical wintertime teleconnections on Northern Hemisphere temperature. *Geophys. Res. Lett.*, **23**, 665–668..

Jiang, S., F.-F. Jin, and M. Ghil, 1995: Multiple equilibria, periodic and aperiodic solutions in a wind-driven, double-gyre, shallow-water model. *J. Phys. Oceanogr.*, **25**, 764–786.. [Find this article online](#)

Jones, D. A., A. C. Poje, and L. G. Margolin, 1997: Resolution effects and enslaved finite-difference schemes for a double gyre shallow-water model. *Theor. Comput. Fluid. Dyn.*, **9**, 269–280..

Kiss, A. 1998: Chaos in the “sliced cone” model of wind-driven ocean circulation. Proceedings of the 1998 Woods Hole Geophysical Fluid Dynamics Program, WHOI Tech. Rep., Woods Hole, MA. [Available from Woods Hole Oceanographic Institution, Woods Hole, MA 02543.].

Kushnir, Y., 1994: Interdecadal variations in North Atlantic sea surface temperature and associated atmospheric conditions. *J. Climate*, **7**, 141–157.. [Find this article online](#)

Legras, B., and M. Ghil, 1985: Persistent anomalies, blocking and variations in atmospheric predictability. *J. Atmos. Sci.*, **42**, 433–471.. [Find this article online](#)

McCalpin, J. D., and D. B. Haidvogel, 1996: Phenomenology of the low-frequency variability in a reduced gravity, quasigeostrophic double-gyre model. *J. Phys. Oceanogr.*, **26**, 739–752.. [Find this article online](#)

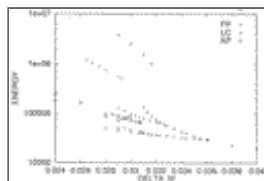
Meacham, S. P., and P. Berloff, 1997: Barotropic wind-driven circulation in a small basin. *J. Mar. Res.*, **55**, 523–563..

Milliff, R. F., W. G. Large, W. R. Holland, and J. C. McWilliams, 1996: The general circulation response of high resolution North Atlantic ocean models to synthetic scatterometer winds. *J. Phys. Oceanogr.*, **26**, 1747–1768.. [Find this article online](#)

Moro, B., 1990: On the nonlinear Munk model. II. Stability. *Dyn. Atmos. Oceans*, **14**, 203–227..

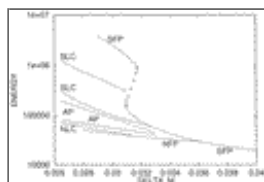
Olson, D. B., G. P. Podesta, R. H. Evans, and O. B. Brown, 1988: Temporal variations in the separation of Brazil and Malvinas Currents. *Deep-Sea Res.*, **35**, 1971–1990..

Figures



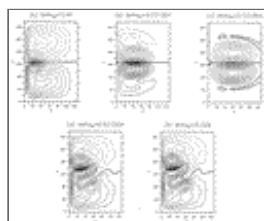
[Click on thumbnail for full-sized image.](#)

Fig. 1. Regime diagram for the symmetric barotropic double-gyre problem. Symbols indicate families of antisymmetric and nonsymmetric steady states (FP), antisymmetric and nonsymmetric limit cycles (LC), and aperiodic solutions (AP).



[Click on thumbnail for full-sized image.](#)

Fig. 2. Sketch of bifurcation curves for symmetric barotropic double-gyre problem. The band marked AP indicates the average energy of aperiodic solutions; SFP indicates branches of antisymmetric steady states; NFP, branches of nonsymmetric steady circulations; SLC, branches of antisymmetric periodic solutions; and NLC, branches of nonsymmetric periodic solutions. Note that for NFP and NLC, a pair of branches of solutions with opposite symmetries map to a single curve on the figure.



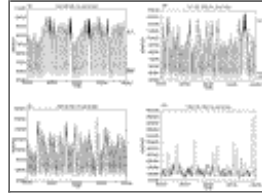
[Click on thumbnail for full-sized image.](#)

Fig. 3. Streamfunction fields of steady-state solutions of the symmetric barotropic double-gyre problem. CI denotes contour interval. (a) $\delta_M = 0.04$, antisymmetric steady state, $CI = 4 \times 10^{-3}$; (b) $\delta_M = 0.031$, low-energy antisymmetric state, $CI = 1 \times 10^{-2}$; (c) $\delta_M = 0.031$, high energy antisymmetric state, $CI = 4 \times 10^{-2}$; (d) $\delta_M = 0.031$, a nonsymmetric state, $CI = 4 \times 10^{-3}$; (e) $\delta_M = 0.029$, a nonsymmetric state, $CI = 4 \times 10^{-3}$.



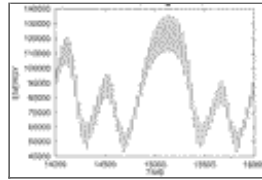
Click on thumbnail for full-sized image.

Fig. 4. A streamfunction example of a nonsymmetric limit cycle, $\delta_M = 0.0314$.



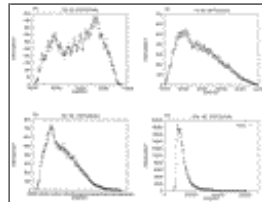
Click on thumbnail for full-sized image.

Fig. 5. Twenty thousand day segments of time series of basin-integrated kinetic energy $K(t)$, from aperiodic solutions: (a) $\delta_M = 0.0307$, (b) $\delta_M = 0.029$, (c) $\delta_M = 0.028$, and (d) $\delta_M = 0.024$. In (a) and (b), NFP denotes the energy of the nonsymmetric fixed points, while NLC and SLC indicate the average energies of the nonsymmetric limit cycles and the lowest energy antisymmetric limit cycle, respectively.



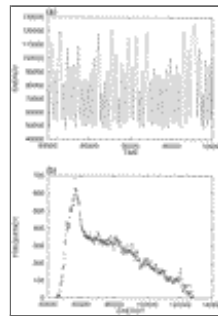
Click on thumbnail for full-sized image.

Fig. 6. Plot of $K(t)$ over a short interval for an aperiodic solution with $\delta_M = 0.029$.



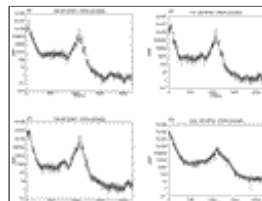
Click on thumbnail for full-sized image.

Fig. 7. Histograms of kinetic energy from 100,000-day segments of the aperiodic solutions shown in [Fig. 5](#).



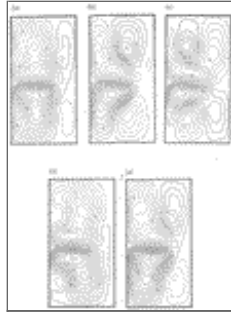
Click on thumbnail for full-sized image.

Fig. 8. (a) A 20,000-day segment of a time series of the running mean of the basin-integrated kinetic energy, $\langle K(t) \rangle$, from an aperiodic solution with $\delta_M = 0.029$. (b) Histogram of smoothed kinetic energy from an aperiodic solution with $\delta_M = 0.029$.



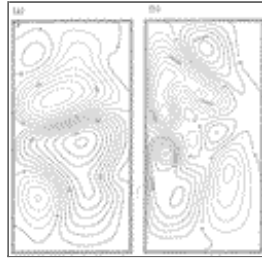
Click on thumbnail for full-sized image.

Fig. 9. Power spectra of basin-integrated kinetic energy time series for (a) $\delta_M = 0.0307$, (b) $\delta_M = 0.029$, (c) $\delta_M = 0.028$, and (d) $\delta_M = 0.024$. A frequency of 10 corresponds to a period of 3277 days.



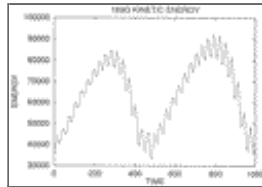
[Click on thumbnail for full-sized image.](#)

Fig. 10. Snapshots of the streamfunction from an aperiodic solution with $\delta_M = 0.029$ at a time when the solution is near one of the high-energy peaks. The snapshots are separated by intervals of 8 days.



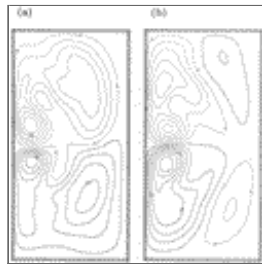
[Click on thumbnail for full-sized image.](#)

Fig. 11. Snapshots of the streamfunction from an aperiodic solution with $\delta_M = 0.024$. (a) At an instant when the basin-integrated kinetic energy is close to a large amplitude maximum value. (b) At a time when the kinetic energy is close to a large amplitude minimum.



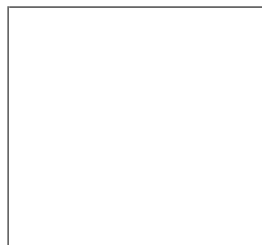
[Click on thumbnail for full-sized image.](#)

Fig. 12. A short segment of $K(t)$ time series from an aperiodic solution with $\delta_M = 0.0307$.



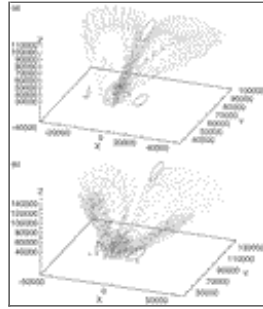
[Click on thumbnail for full-sized image.](#)

Fig. 13. Snapshots of streamfunction from an aperiodic solution with $\delta_M = 0.0307$ when the solution is in a low energy trough. The interval between snapshots is 16 days.



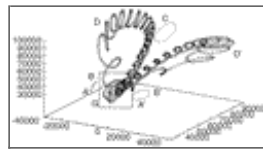
Click on thumbnail for full-sized image.

Fig. 14. Snapshots of streamfunction from an aperiodic solution with $\delta_M = 0.0307$ when the solution is at a peak of the large amplitude vacillation cycle. The interval between snapshots is 16 days.

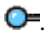


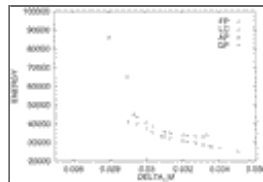
Click on thumbnail for full-sized image.

Fig. 15. Projections of two aperiodic solutions onto an artificial three-dimensional phase space. The aperiodic trajectories are shown as dotted curves. Also shown are nonsymmetric limit cycles (the two closed solid curves at low Z values), the low energy antisymmetric limit cycle (the closed solid curve on the X = 0 plane at higher Z values), and the nonsymmetric steady states (marked with diamonds). See the text for definitions of the coordinates. (a) $\delta_M = 0.0307$ and (b) $\delta_M = 0.029$.



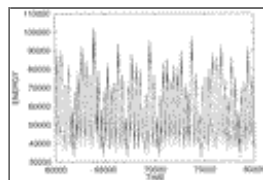
Click on thumbnail for full-sized image.

Fig. 16. Sketch of the behavior of the aperiodic trajectories shown in [Fig. 15](#) .



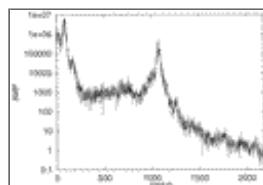
Click on thumbnail for full-sized image.

Fig. 17. Bifurcation diagram for the asymmetrically forced barotropic double gyre with $r = 0.9$. FP: steady circulations, LC: periodic solutions, QP: toroidal attractors, and AP: aperiodic solutions.



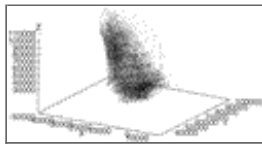
Click on thumbnail for full-sized image.

Fig. 18. A segment of a time series of basin-integrated kinetic energy from an aperiodic solution of the asymmetrically forced barotropic double gyre problem. ($r = 0.9$, $\delta_I = 0.04$, $\delta_M = 0.029$).



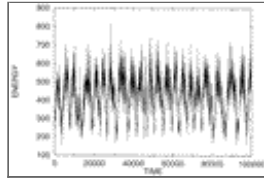
Click on thumbnail for full-sized image.

Fig. 19. The power spectrum of a time series of basin-integrated kinetic energy, $K(t)$, from an aperiodic solution of the asymmetrically forced barotropic double gyre problem ($r = 0.9$, $\delta_I = 0.04$, $\delta_M = 0.029$). A frequency of 10 corresponds to a period of 3277 days.



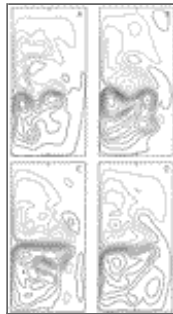
Click on thumbnail for full-sized image.

Fig. 20. A projection of a longer segment of the aperiodic solution shown in [Fig. 18](#) onto an artificial three-dimensional phase space.



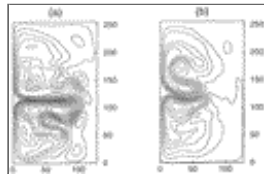
Click on thumbnail for full-sized image.

Fig. 21. A 100 000-day segment of a time series of the kinetic energy of the flow in the upper layer of a two-layer, asymmetrically forced, double-gyre model, integrated over the horizontal extent of the basin ($r = 0.85$, $\delta_I = 0.04$, $\delta_M = 0.02$).



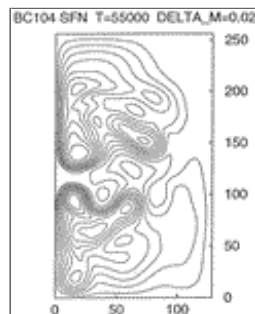
Click on thumbnail for full-sized image.

Fig. 22. Four random snapshots of the upper-layer streamfunction from the solution shown in [Fig. 21](#).



Click on thumbnail for full-sized image.

Fig. 23. Plots of instantaneous upper-layer streamfunction taken from the solution shown in [Fig. 21](#) at (a) a time during a peak and (b) a time during a trough of the large amplitude vacillation in energy.



Click on thumbnail for full-sized image.

Fig. 24. A plot of instantaneous upper-layer streamfunction from the run shown in [Fig. 21](#) at a time when the subpolar and subtropical gyres have separated.





[Click on thumbnail for full-sized image.](#)

Fig. 25. Power spectrum of the time series of basin-integrated upper-layer kinetic energy shown in [Fig. 21](#). A frequency of 10 corresponds to a period of 3277 days.

¹ Stationary and Hopf bifurcations of the double-gyre model were also examined by [Dijkstra and Katsman \(1997\)](#).

² Recent published and unpublished results from laboratory models of circulation in sliced cylinders and sliced cones by [Griffiths and Veronis \(1997\)](#) and [Kiss \(1998\)](#) also show evidence of Hopf bifurcations from steady to periodic and eventually more complicated regimes. Additional evidence for this comes from numerical modeling of the laboratory experiments carried out by [Kiss \(1998\)](#).

Corresponding author address: Dr. S. P. Meacham, Atmospheric and Environmental Research, Inc., 840 Memorial Drive, Cambridge, MA 02139-3771.

E-mail: steve@pimms.mit.edu

[top](#) ▲



© 2008 American Meteorological Society [Privacy Policy and Disclaimer](#)
Headquarters: 45 Beacon Street Boston, MA 02108-3693
DC Office: 1120 G Street, NW, Suite 800 Washington DC, 20005-3826
amsinfo@ametsoc.org Phone: 617-227-2425 Fax: 617-742-8718
[Allen Press, Inc.](#) assists in the online publication of AMS journals.